

Open-state structure of veratridine-activated human Na_v1.7 reveals the molecular choreography of fast inactivation

Xiao Fan^{*1#}, Jiaofeng Chen^{2#}, Lingfeng Xue^{3#}, Huan Wang², Tong Wu², Xiaoshuang Huang¹, Fangzhou Lu¹, Xueqin Jin², Chen Song^{*3}, Jian Huang^{*1}, Nieng Yan^{*1,2,4}

Nearly all the reported cryogenic electron microscopy (cryo-EM) structures of eukaryotic voltage-gated sodium (Na_v) channels, including those of human Na_v1.1–Na_v1.8, represent various inactivated states, with the characteristic of a non-conductive pore domain surrounded by voltage-sensing domains in varying activated conformations. To capture an open-state Na_v structure, we treated human Na_v1.7 with a natural neurotoxin veratridine (VTD). Cryo-EM structures of two complexes of VTD-bound Na_v1.7 were obtained at overall resolutions of 2.7 Å and 2.9 Å. One, with VTD inserted in the IFM-binding pocket (site I), resembles other inactivated structures; the other, wherein VTD traverses the central cavity (site C), represents an activated conformation with a constriction diameter of 8.2 Å at the intracellular gate. Structural analysis reveals the molecular basis of the bimodal modulation of Na_v channels by VTD. More importantly, comparison of the open and inactivated structures elucidates the precise molecular process of fast inactivation in Na_v channels.

<https://doi.org/10.15302/vita.2026.01.0003>

INTRODUCTION

In multicellular organisms, electrical signaling is indispensable for nearly all neuronal activities and a wide range of physiological processes^{1–3}. Voltage-gated sodium (Na_v) channels govern the initiation and transmission of electrical signals in the form of action potentials in excitable systems such as neurons and muscles. Na_v channels activate upon membrane depolarization, followed by fast inactivation that ensures the repetitive and directional firing of action potentials^{1–3}. Following decades of rigorous investigation into their physiological and pathophysiological roles, recent investigations have mainly been focused on elucidating the structure–function relationship of Na_v channels. The technological breakthrough in single-particle cryogenic electron microscopy (cryo-EM) has led to the structural determination of human Na_v1.1–Na_v1.8^{3–8}.

Most of the mammalian Na_v structures captured to date represent inactivated states, which are featured with a non-conductive pore domain (PD), depolarized or “up” voltage-sensing domains (VSDs), and the fast inactivation motif, Ile/Phe/Met (IFM), wedged in the receptor site adjacent to the intracellular gate³. Towards an in-depth and comprehensive understanding of their working mechanisms, structural snapshots of Na_v channels in all major states are indispensable. The structure of Na_v channels in the activated or resting state remains to be determined.

Many strategies have been employed to lock the purified Na_v channels in distinct conformations. Certain peptide toxins successfully trap VSD_{IV} in a down conformation, but the other three VSDs and PD remain unchanged^{9,10}. One structure of a rat Na_v1.5 mutant rNa_v1.5-QQQ, in which the IFM motif was

replaced by Gln/Gln/Gln, was announced to be the open state in the presence of the open-pore blocker propafenone¹¹. However, there is a key mismatch between the structural model and the 3D EM reconstruction. As will be elaborated later, our molecular dynamics simulation (MDS) analysis of the original and corrected structures of rNa_v1.5-QQQ suggested that neither could be conductive.

To probe Na_v gating transitions, we engineered a series of point mutations to modulate the voltage dependence of activation and inactivation of Na_v1.7 channels^{12,13}. In the structure of Na_v1.7-M11, a mutant that contains eleven rationally designed single point mutations, VSD_I displays a completely down conformation and the PD is in a tightly contracted state, lacking the fenestrations seen in other inactivated Na_v structures¹². Electrophysiological characterizations suggest that the structure of Na_v1.7-M11 may represent a closed-state inactivation (CSI) conformation. The structural study of Na_v1.7-M11 demonstrates the feasibility of capturing Na_v1.7 in distinct functional states. In fact, Na_v1.7 has been more extensively characterized structurally than other subtypes, due in part to the well-established genetic evidence linking it to pain sensation and subsequent efforts targeting it for analgesic development^{14–17}. Since 2019, more than twenty human Na_v1.7 structures have been determined in complex with diverse modulators^{3,12,13,18–23}. Na_v1.7 also yields the highest resolution for any Na_v structures, at 2.2 Å for the overall structure¹⁹.

Encouraged by these results, we continued to focus on human Na_v1.7 with the goal of determining its structures in both resting and activated states. In an attempt to determine

1. Institute of Bio-Architecture and Bio-Interactions (IBABI), Shenzhen Medical Academy of Research and Translation (SMART), Guangming District, Shenzhen, Guangdong, China. 2. Beijing Frontier Research Center for Biological Structures, State Key Laboratory of Membrane Biology, Tsinghua-Peking Joint Center for Life Sciences, School of Life Sciences, Tsinghua University, Beijing, China. 3. Center for Quantitative Biology, Academy for Advanced Interdisciplinary Studies, Peking University, Beijing, China. 4. Institute of Chemical Biology (ICB), Shenzhen Bay Laboratory, Guangming District, Shenzhen, Guangdong, China. #These authors contribute equally. *Correspondence: Xiao Fan (xfan@smart.org.cn), Chen Song (c.song@pku.edu.cn), Jian Huang (huangjian@smart.org.cn), Nieng Yan (nyan@tsinghua.edu.cn)

Received: December 3, 2025; Accepted: January 20, 2026; Published: January 25, 2026

the structure of Na_v1.7 in the activated state, we treated the channel with veratridine (VTD), an alkaloid neurotoxin derived from the lily family that is known to act as a potent Na_v opener²⁴⁻²⁶. VTD preferentially binds the activated sodium channel, inducing a hyperpolarizing shift. This promotes channel opening at more negative potentials and delays inactivation, leading to more persistent activation at resting membrane potential²⁴⁻²⁶. On the other hand, VTD binding lowers the peak current; single-channel recordings show reduced conductance^{27,28}.

Here, we report the cryo-EM structures of wild-type (WT) Na_v1.7 in two distinct conformations, each with one VTD bound. The structure of Na_v1.7 with VTD standing near the IFM motif, defined as site I (I for inactivation), is reminiscent of the cannabidiol (CBD)-bound, inactivated state²². The other structure, where the elongated steroidal alkaloid VTD traverses the spacious cavity of the PD (site C), appears to represent the activated conformation with all four VSDs in the up state and an open pore. This open-state structure reflects a potentially conductive conformation in our MDS analysis. Structural comparison of Na_v1.7 in the activated and inactivated states elucidates the dynamic details for fast inactivation, and reveals the pathogenic mechanism for dozens of disease-related mutations.

RESULTS

Distinct structures of Na_v1.7 treated with VTD

Prior to the cryo-EM analysis of VTD in complex with human Na_v1.7, we validated the functional effects of the purchased VTD. Human Na_v1.7 channels, WT or mutants, were transiently expressed in HEK293T cells for whole-cell patch-clamp electrophysiological recordings, treated with VTD under different conditions.

With standard steady-state activation and inactivation protocols (see Materials and Methods), VTD induced a pronounced hyperpolarizing shift in both activation and inactivation curves (Supplementary Fig. S1 and Tables S1-S4). In the meantime, it suppressed the peak current amplitude in a dose-dependent manner, with an IC₅₀ of 92.7 ± 18.4 μM (Fig. 1a). VTD also elicited a persistent inward current and a prominent tail current, both of which were enhanced with increasing concentrations of VTD (Fig. 1a, left). To amplify these small-amplitude currents and probe VTD's use-dependent modulation, we applied a 5-Hz pulse protocol. Upon repetitive depolarizations, VTD produced cumulative peak current inhibition and enhanced tail current induction, yielding an EC₅₀ for the tail current of 95.4 ± 16.6 μM (Fig. 1a, middle and right). The distinctive bimodal modulation of suppression of peak current and induction of persistent and tail currents is consistent with the reported effects of VTD on Na_v channels²⁹.

For structural determination, we co-expressed human Na_v1.7 with auxiliary β1 and β2 subunits and conducted protein purification and cryo-sample preparation following an established workflow^{12,18}. Considering the limited solubility, VTD was included throughout the purification process to ensure sufficient channel occupancy. When VTD was applied at 100 μM, three major classes of reconstructions were obtained after cryo-EM data acquisition and processing (Supplementary Figs. S2, S3, and Table S5). One class has no VTD density, representing an apo form that is identical to the reported WT structure¹⁹ (Supplementary Fig. S3e). In another class, the density that clearly belongs to a VTD molecule

stands next to the IFM motif (Supplementary Figs. S3d, S4). The overall structure remains similar to the apo channel, with a root-mean-square deviation (RMSD) of 0.96 Å over 1,244 Ca atoms in the α subunit when superimposed in PyMOL³⁰ (Fig. 1b). Local shifts occur in the cytosolic tip of S6_{III} as a result of the insertion of the VTD molecule (Fig. 1b, right). Based on our recently proposed definition for ligand binding sites on Na_v and Ca_v channels, this VTD binds to site I^{21,31}. We refer to this structure as Na_v1.7V_I, which features an inactivated state.

The last class displays marked changes in VTD binding and channel conformation. The elongated VTD molecule traverses the entire central cavity (site C), with its 4,9-epoxycevan and 3,4-dimethoxybenzoate ends pointing to fenestrations I-II and III-IV, respectively (Fig. 1c). We will call this structure Na_v1.7V_O. As will be demonstrated later, the intracellular gate is sufficiently widened in this conformation to conduct Na⁺. Unlike CBD, lacosamide, and lamotrigine, each of which simultaneously binds to two sites on the PD²¹⁻²³, the pore states in class I and class O are different, suggesting exclusive binding of VTD to site I or site C in these two conformations.

Similar binding poses of VTD and CBD at site I

The overall structure of Na_v1.7V_I is similar to the CBD-bound one, with an RMSD of 0.92 Å over 1,239 Ca atoms (Fig. 2a; Supplementary Fig. S4a). As aforementioned, two CBD molecules simultaneously bind to the PD of Na_v1.7, one penetrating the fenestration (site F) and the other fortifying the IFM binding site by standing next to Ile and Phe²². In Na_v1.7V_I, only one VTD is observed in the PD. The 3,4-dimethoxybenzoate moiety inserts into the corner enclosed by S4-5_{III}, S6_{III}, and S6_{IV}, surrounded mostly by hydrophobic residues. The remaining portion of the molecule, containing the cevanine skeleton, projects toward the cytosol (Fig. 2a, b). This binding pose is compatible with its higher aqueous solubility conferred by several hydroxy groups.

Consistent with the similar binding poses at site I, both VTD and CBD reduce the peak currents and stabilize an inactivated state, the latter manifested by the leftward shift of the voltage-dependence for steady-state inactivation (Supplementary Fig. S1)²². As the mechanism of action of modulators associated with site I has been elaborated in our previous work^{22,31,32}, we refrain from repeating these details in the current work, but focus on the other binding pose of VTD.

Gate opening upon VTD binding to site C

In Na_v1.7V_O, VTD, along its long axis, is closer to repeats II and III (Fig. 3a, left panel). The molecule is coordinated through extensive hydrophobic and polar interactions. S6_{III} engages four residues, Ser1445, Thr1448, Leu1449, and Phe1452, more than any other individual segments (Fig. 3a; Supplementary Fig. S4b). Leu393 and Ile397 on S6_I, Leu960 on S6_{II}, Trp1332 on S5_{III}, and Ile1745 on S6_{IV} contribute to the van der Waals contacts with VTD. The C-terminal residues of the P1 helices in repeat I-III, Thr359, Cys925, and Ala1403, all use their backbone carbonyl oxygen to hydrogen (H)-bonded with the hydroxyl groups of VTD. Phe1405 on the selectivity filter (SF) loop in repeat III also participates in VTD binding (Fig. 3a, right panels).

The PD of Na_v1.7V_O is evidently dilated. Calculation of the radii of the permeation path reveals a constriction site diameter of 8.2 Å, sufficient to permeate a 7.2-Å hydrated Na⁺ ion (Fig. 3b). By comparison, the gate for WT apo channel is 5.0 Å (Fig. 3b). Previously, structural study of rNa_v1.5-QQQ

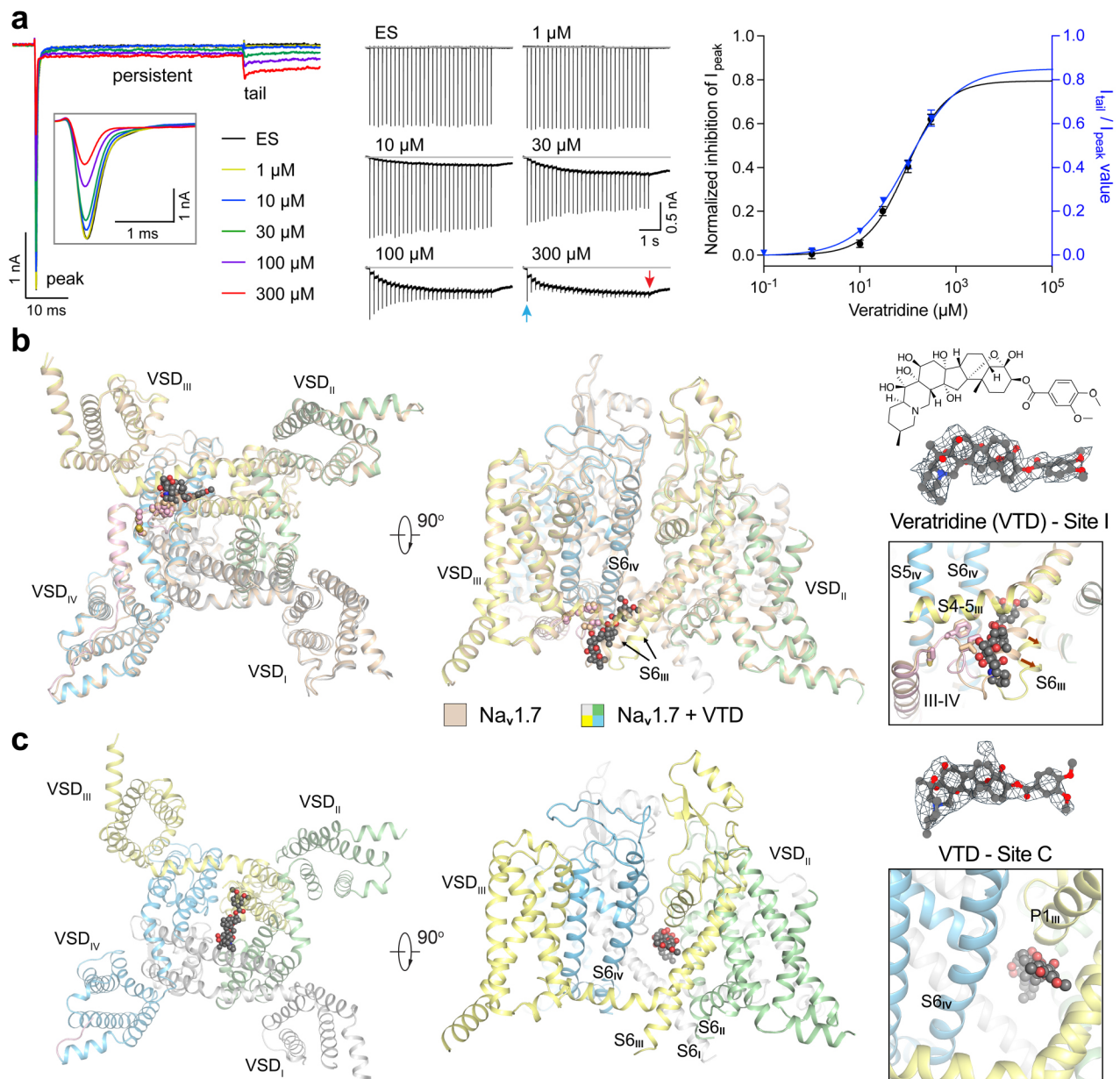


Fig. 1 Bimodal regulation of $\text{Na}_v1.7$ by VTD may be explained by the dual binding poses on the PD. **a** Use-dependent inhibition of $\text{Na}_v1.7$ peak current and enhancement of its tail current by VTD. Left: Representative traces showing the effects of indicated concentrations of VTD on $\text{Na}_v1.7$ peak, persistent, and tail currents. Cells were held at -120 mV and depolarized to a test pulse to 0 mV for 50 ms. An enlarged view of the peak current is shown in the inset. ES, external solution. Middle: Representative traces illustrating the use-dependent modulation of $\text{Na}_v1.7$ currents, evoked by a 5 -Hz train stimulation (30 pulses of 5 -ms duration from -120 mV to 0 mV). The accumulated tail current (red arrow) was measured and normalized to the amplitude of the first peak current (blue arrow), with both values corrected against the baseline (grey line). Right: Concentration-response relationships for VTD-mediated inhibition of $\text{Na}_v1.7$ peak current (black curve, $\text{IC}_{50} = 92.66 \pm 18.41 \mu\text{M}$, $n = 13, 17, 16, 15, 15$) and enhancement of the accumulated tail current (blue curve, $\text{EC}_{50} = 95.44 \pm 16.62 \mu\text{M}$, $n = 18, 10, 12, 13, 13, 11$). Data are presented as mean \pm SEM. Details are presented in the Materials and Methods and Supplementary Tables S1–S4. **b**, **c** Three classes of $\text{Na}_v1.7$ cryo-EM structures were obtained when treated with $100 \mu\text{M}$ VTD, including apo and two binding poses for VTD. **b** The $\text{Na}_v1.7V_I$ structure, in which a VTD binds next to the fast inactivation IFM motif, shares a largely similar conformation with the apo channel. We have named this ligand-binding site on Na_v channels the site I. Structures of $\text{Na}_v1.7V_I$ (colored by repeats) and the apo channel (colored wheat) can be superimposed with the RMSD of 0.96 \AA over $1,244$ Ca pairs. The major local shift near site I is highlighted by red arrows in the inset. **c** In class O, a VTD traverses the central cavity (site C). The VTD densities, shown as grey meshes in ChimeraX⁴⁶, are contoured at 6σ . All structure figures, if not otherwise indicated, were prepared in PyMOL⁵⁰.

suggested an open gate (Fig. 3b). However, re-examination of its deposited map (EMD-31519) and structural coordinates (PDB: 7FBS) revealed an error in model building (Supplementary Fig. S5). An incorrectly assigned π -helix at segment S_5 :400–403 induces a positional shift of all the residues downstream of Gly401, resulting in inaccurate analysis of the permeation path (Supplementary Fig. S5a).

We rebuilt and refined the PD of r $\text{Na}_v1.5$ -QQQ against the deposited map. The updated coordinates (r $\text{Na}_v1.5$ -QQQ-

rebuild) substantially improved model fitting to the density map and enhanced model quality metrics across all validation parameters (Supplementary Fig. S5d). In r $\text{Na}_v1.5$ -QQQ-rebuild, the segment S_5 :390–429 shows an RMSD of 3.3 \AA over 40 Ca atoms compared to the original model, and the rest of the PD remains nearly identical, with an RMSD of 0.4 \AA over 542 Ca atoms. The gate diameter of the rebuilt model is 5.6 \AA , slightly smaller than that of the original model, 6.2 \AA (Supplementary Fig. S5e). The rebuilt r $\text{Na}_v1.5$ -QQQ model will

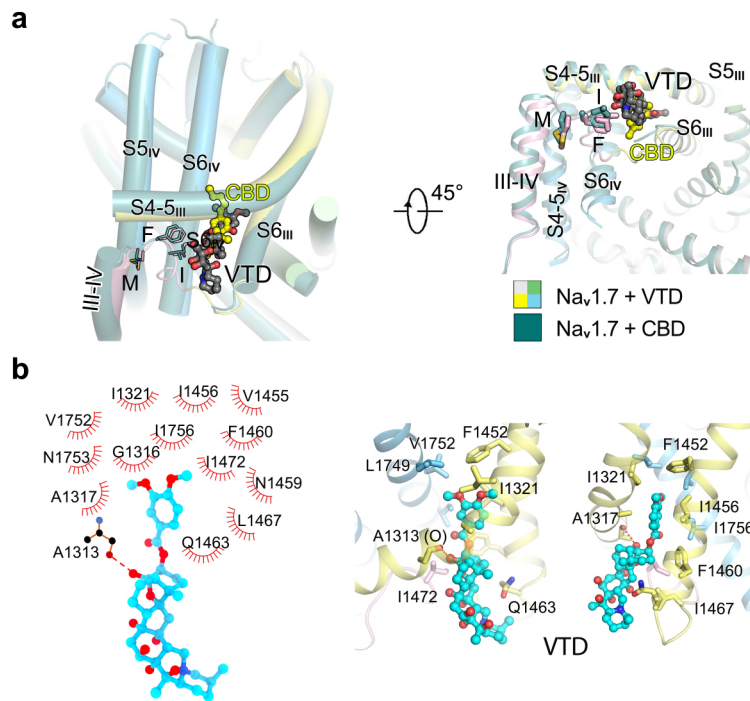


Fig. 2 Site I binding contributes to the antagonistic effect of VTD on Na_v channels. **a** Similar binding poses of VTD and CBD at site I. The structure of Na_v1.7V_I can be superimposed on the CBD-bound one with an RMSD of 0.92 Å across all 1,239 Cα pairs. A tilted side view and a cytosolic view of their superimposed PD structures are shown. The IFM motif is shown as sticks. The PDB code for CBD-bound Na_v1.7 is 8G1A. **b** Coordinating details of VTD at site I. Residues within 4.0 Å of the VTD molecule are displayed in eyelash scheme. The potential H-bonds are indicated with red dashed lines. Left: A schematic illustration of the binding details of VTD at site I. Middle and Right: Two side views of VTD coordination. VTD is shown as cyan ball and sticks, and the surrounding residues are shown as sticks.

be used for all major comparisons and analyses unless otherwise stated.

HOLE analysis confirms that, among all publicly available Na_v structures, Na_v1.7V_O presented in this study is the only one with the gate diameter large enough to potentially allow the permeation of hydrated Na⁺ ions. We will present the MDS characterization of the open pore in the next section. In the following, we examine the mechanism by which VTD dilates the channel.

The two classes of VTD-bound structures can be superimposed with an RMSD of 1.2 Å over 1,180 aligned Cα pairs. Despite the prominent structural deviations of the PD segments, most of the VTD-coordinating residues remain nearly unchanged at site C, except those on S6_{iii}. In particular, Thr1448 and Leu1449 would sterically clash with VTD without a major displacement (Fig. 3c). Of note, Ala substitution of Thr1448 would still need to undergo the conformational changes to avoid the clash between VTD and the Cβ atom. By contrast, replacement of Leu1449 by Ala may avoid the steric clash even when the PD is contracted as in the apo or class I state. Along this line of thinking, Ala substitution of Leu960, a residue on S6_{ii} that anchors the other end of VTD, may also provide extra space to accommodate VTD in the absence of a major shift of S6_{iii}.

To test this analysis, we generated Na_v1.7 mutants with single-point mutations, L960A, T1448A or L1449A. Whereas T1448A had no significant effect on the bimodal regulation of Na_v1.7 by VTD, both L960A and L1449A led to a nearly complete loss of both the persistent and tail currents (Fig. 3d; Supplementary Figs. S6, S7). Meanwhile, these two mutations each rendered Na_v1.7 more sensitive to VTD inhibition, which was especially evident in the use-dependent measurement (Fig. 3d-g; Supplementary Fig. S6). Therefore, Leu960 and Leu1449 appear to be two key residues that couple the

site C binding of VTD to pore opening. Interestingly, according to our recently proposed versatile residue numbering scheme for Na_v channels³³, these two key residues (Leu960_{S6ii,29}; Leu1449_{S6iii,29}) are located at the corresponding positions on S6_{ii} and S6_{iii}, respectively.

Open conformation of the intracellular gate in Na_v1.7V_O

In the 3D EM map of Na_v1.7V_O, the IFM-containing III-IV linker (residues 1465–1497) is completely invisible. Compared to the IFM-loaded apo Na_v1.7 structure, the fenestration on the interface of repeats III and IV is directly connected to the intracellular gate, leaving a wide cleft (Fig. 4a). We performed MDS of PD in Na_v1.7V_O, with VTD removed, to examine whether the substantially widened gate is permeable to hydrated Na⁺ ions. The PDs of WT human Na_v1.7 and the original and rebuilt rNa_v1.5-QQQ were analyzed in parallel.

The simulations of PDs were conducted under a transmembrane potential of 120 mV. The intracellular gate is fully hydrated in the Na_v1.7V_O structure (Supplementary Video S1). Consistently, ion permeation analysis confirmed the permeation of Na⁺ ions with a calculated conductance of 13.8 ± 5.0 pS, which is comparable to the experimental value³⁴ (Fig. 4d; Supplementary Video S1). In contrast, the apo WT hNa_v1.7 and the two rNa_v1.5-QQQ structures exhibited minimal hydration at the corresponding region, unable to permeate Na⁺ ions in our MDS analysis (Fig. 4b, c; Supplementary Video S1).

We also characterized the dynamic process of Na⁺ permeation through the channel (Fig. 4e). Na⁺ ions remained hydrated as they passed through the intracellular gate (Supplementary Video S1). Furthermore, trajectory analysis showed an asymmetric path for the Na⁺ ions, which are preferentially located near S6_{iv} and the wide cleft between S6_{iii} and S6_{iv} (Fig. 4f).

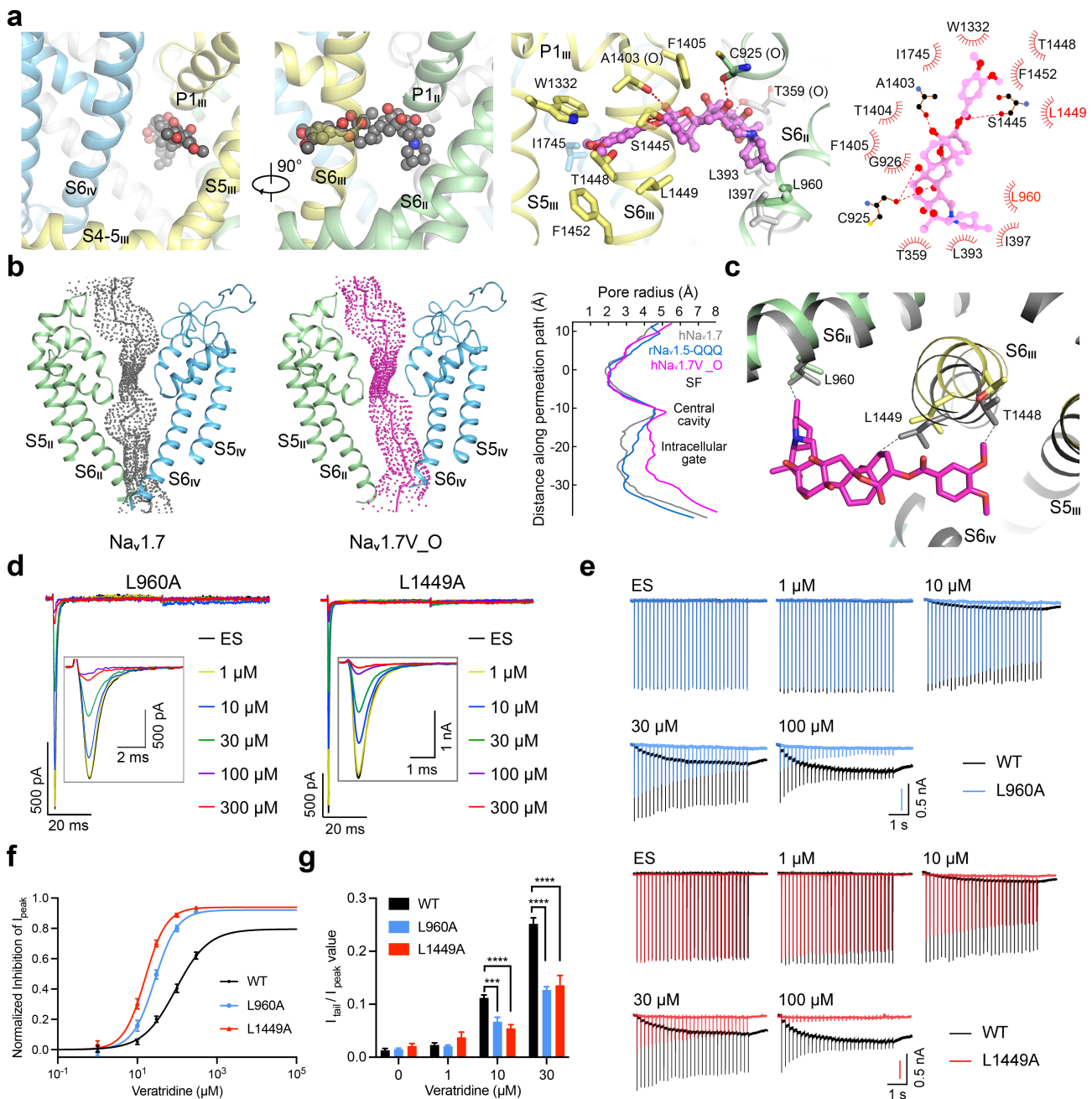


Fig. 3 VTD binding at site C opens the pore. **a** Coordination of VTD in the central cavity. Left two panels: Two perpendicular views, in addition to that in Fig. 1c, to illustrate the binding pose of VTD at site C. Right two panels: Details of VTD binding. Coordinating residues are shown as sticks. **b** The pore is substantially dilated in the presence of VTD at site C. The permeation path of the PD (VTD omitted) is calculated using HOLE⁴⁷. The radii of the permeation path in the indicated structures are shown on the right. The original error in the model building of the reported structure rNa_v1.5-QQ¹¹ and the correction are described in Supplementary Fig. S5. **c** The S6_{III} segment appears to play a major role in coupling VTD binding to pore opening. VTD would clash with Thr1448 and Leu1449 if S6_{III} had not shifted outward substantially. The black, dashed lines indicate potential clashes between VTD groups and the two residues. **d–g** Functional validation of the structural analysis. Two single-point mutations, L960A and L1449A, enhance VTD-mediated inhibition and nearly abolish its pore-opening effect on Na_v1.7. **d** Shown here are representative traces for the measurement of VTD on Na_v1.7-L960A (left) and Na_v1.7-L1449A (right) currents. The protocol is the same as for the WT channel. Cells were held at -120 mV and depolarized to a test pulse to 0 mV for 50 ms. An enlarged view of the peak current is shown in the inset. **e** Representative traces illustrating the use-dependent modulation of VTD on Na_v1.7-L960A (top, blue) and Na_v1.7-L1449A (bottom, red) compared to Na_v1.7-WT (black) currents, evoked by a 5-Hz train stimulation (30 pulses of 5-ms duration from -120 mV to 0 mV). The currents for Na_v1.7-WT are the same as in Fig. 1a. **f** Concentration-response relationships for VTD-mediated peak current inhibition of Na_v1.7-L960A and Na_v1.7-L1449A compared to Na_v1.7-WT. IC₅₀ = 92.66 ± 18.41 μM, n = 13, 17, 16, 15, 15 for Na_v1.7-WT; IC₅₀ = 27.56 ± 2.30 μM, n = 10, 10, 11, 10, 7 for Na_v1.7-L960A; IC₅₀ = 15.68 ± 0.97 μM, n = 9, 10, 10, 8, 8 for Na_v1.7-L1449A. **g** Quantitative analysis of accumulated tail currents normalized to the first peak current of the train stimulation for Na_v1.7-L960A, Na_v1.7-L1449A, and Na_v1.7-WT. Data were analyzed by one-way ANOVA; ***P < 0.001, ****P < 0.0001. Experimental details are presented in Materials and Methods and Supplementary Tables S1–S4.

Structural basis for fast inactivation

We previously, in the absence of an open structure, suggested that the IFM motif might execute a fast cutoff of the ion flow mainly through pushing S6_{IV} to close the intracellular gate^{7,8}. Determination of an open structure of Na_v1.7

fills a critical void in understanding the process of fast inactivation and offers an updated view on the cascade of molecular events that complete the fast inactivation in Na_v channels.

When the structures of Na_v1.7V_O and the apo channel are overlaid, there is nearly no change in their VSDs, all of which

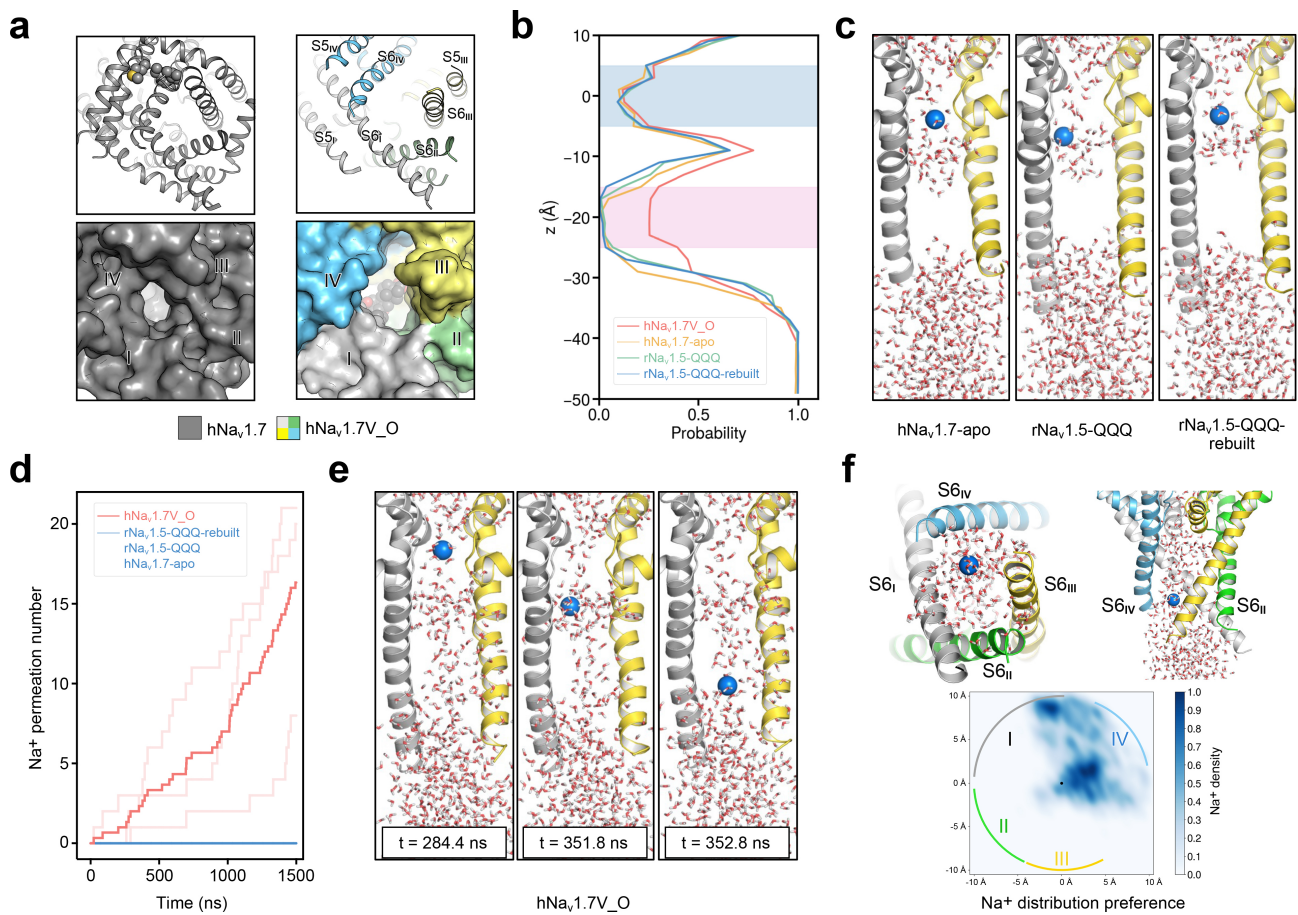


Fig. 4 MDS analyses confirm the conductive state of $\text{Na}_v1.7\text{V}_\text{O}$. **a** A cleft along the interface of S6_{III} and S6_{IV} is contiguous with the intracellular gate in $\text{Na}_v1.7\text{V}_\text{O}$. Shown here are identical intracellular views of the PD in the apo and class O structures. Cartoon and surface presentations of identical views are shown on the top and bottom, respectively. **b** Density distribution of water molecules along the z-axis within the central pore of the indicated channel structures. Results are shown for $\text{hNa}_v1.7\text{V}_\text{O}$ (red), $\text{hNa}_v1.7$ apo (orange), $\text{rNa}_v1.5\text{-QQQ}$ (green), and $\text{rNa}_v1.5\text{-QQQ-rebuilt}$ (blue). Selectivity filter and intracellular gate regions are shaded in blue and pink, respectively. **c** Molecular visualization of the hydration state of different channels from selected simulation frames at 1500 ns ($\text{hNa}_v1.7\text{-apo}$) or 600 ns ($\text{rNa}_v1.5\text{-QQQ}$ and $\text{rNa}_v1.5\text{-QQQ-rebuilt}$). For visual clarity, only repeat I and repeat III in the PD are displayed. Sodium ions are depicted as blue spheres, and water molecules are shown as red-and-white sticks. **d** Representative ion permeation events in our MDS analysis of the indicated channel structures. The three light red lines represent three independent simulations of the $\text{hNa}_v1.7\text{V}_\text{O}$ structure, and the dark red line represents the averaged result. As not a single ion permeation event was observed in any of the three replicate simulations for apo $\text{Na}_v1.7$, the original or corrected $\text{rNa}_v1.5\text{-QQQ}$, the corresponding curves are merged and appear as one single blue line. The simulation timestamps are indicated in each panel. **e** Sequential snapshots of a representative ion permeation event through $\text{hNav}1.7\text{V}_\text{O}$. The simulation timestamps are indicated in each panel. **f** Off-axis ion permeation path. Top: A representative snapshot illustrating the angular preference of Na^+ ions as they permeate through the intracellular gate of the $\text{hNa}_v1.7\text{V}_\text{O}$ structure. A bottom and a side view of the same snapshot are shown. Bottom: Projected two-dimensional distribution of Na^+ ions around the S6 gate to the membrane plane. The shaded areas indicate the S6 regions of repeats I-IV, which are colored gray, green, yellow, and blue, respectively. Also see Materials and Methods for details.

exhibit the depolarized or up conformations (Fig. 5a, left). By contrast, the S5 and S6 segments and the S4-5 constriction ring in all four repeats undergo structural changes to varying degrees (Fig. 5a, right). In all the available Na_v structures, including $\text{Na}_v1.7\text{V}_\text{O}$, the SF and its supporting P1, P2, and the upper halves of S5 and S6 segments remain rigid (Fig. 5b). We will hereafter refer to this region as the PD shoulder.

Superimposition of $\text{Na}_v1.7\text{V}_\text{O}$ and the apo structures relative to the shoulder shows tilt of the S6 segments in repeats II-IV, all starting around the fourth helical turn. Note that in repeats I-III, a conserved Gly is positioned on this helical turn, likely representing the key residue that provides the flexibility for the downstream segment (Fig. 5b). At first sight, the cytosolic half of S6_{III} undergoes the most marked displacement, with the C α atom of the cytosolic tip moving by 8.0 Å; those of S6_{IV} and S6_{II} are displaced by 4.5 Å and 4.3 Å, respectively; S6_{I} seems to be nearly unchanged (Fig. 5a, right). Scrutiny of the structure shows that the fourth helical turn in S6_{I} undergoes an $\alpha \rightarrow \pi$ relaxation from the open to the inacti-

vated state, an important structural shift that reorganizes the inner wall of the pore cavity (Fig. 5b).

Then what are the determinants that lead to the structural re-arrangement of the pore-forming segments? When the IFM motif is accessing the receptor site, the Phe residue, which would clash with Asn1753 and Ile1756 on S6_{IV} , directly pushes Ile1756 toward the S6_{I} segment (Fig. 5c, upper inset). Meanwhile, the dragging force exerted by the shift of the III-IV helix, a process that has been analyzed by us and others previously^{7,10,35}, and the van der Waals attractions of Phe1460 on S6_{III} to the Ile and Phe residues in IFM together pull the cytoplasmic terminus of S6_{III} toward S6_{IV} .

The displacements of S6_{III} and S6_{IV} have a profound effect on the pore conformation. Concerted pushing of S6_{IV} and pulling of S6_{III} collectively narrows the intracellular gate, making it impermeable to Na^+ ions (Fig. 5a, right). The side cleft between S6_{III} and S6_{IV} in the open pore is now stitched by an array of hydrophobic residues, only leaving a small fenestration on the interface of repeats III and IV (Fig. 5d,

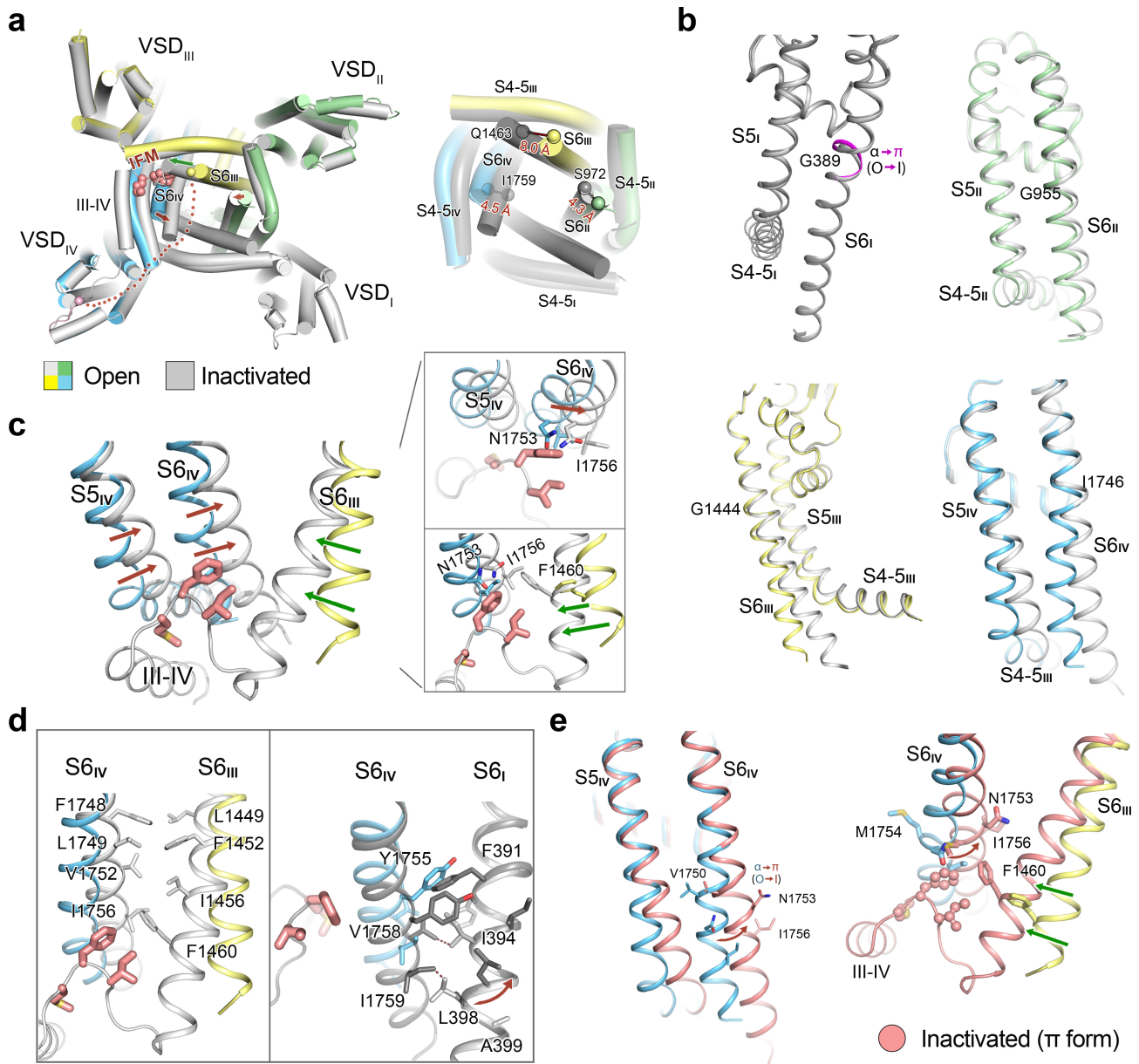


Fig. 5 Structural changes between the open and fast-inactivated Na_v1.7. **a** Cytosolic view of superimposed open and inactivated Na_v1.7. Conformational shifts of the pore-forming segments associated with IFM-induced gate closure. In the open Na_v1.7 structure, the III-IV linker (indicated by the red dotted line), including the IFM motif, is invisible. Structural superimposition of the open and inactivated (apo WT) Na_v1.7 relative to the upper half of the PD reveals differential shifts of the S6 and S4-5 segments in the four repeats, as highlighted in the enlarged view on the right. **b** The pore-forming segments in the four repeats undergo distinct shifts to various extents upon fast inactivation. While the cytosolic halves of the S6 segments in repeats II, III, and IV swing to different extents, S6_I has an $\alpha \rightarrow \pi$ transition in its middle helical turn. The deviation locus in each S6 segment is labelled. Structures of the open and inactivated Na_v1.7 are superimposed as in **a**, and the pore-forming segments in the four repeats are displayed in the views that best reflect their respective deviations. **c** The IFM motif pulls S6_{III} and pushes S6_{IV} to close the intracellular gate. When the hydrophobic IFM motif wedges into the corner between the S4-5_{III} and S4-5_{IV} segments, it exerts two opposing forces. On one side, a potential clash between the Phe residue with Ile1756 pushes S6_{IV} toward S6_I (upper inset, brown arrows). On the other side, it pulls S6_{IV} toward S6_{III} (lower inset, green arrows), resulting in the formation of a hydrophobic core between Ile1756 on S6_{IV} with the Ile and Phe residues in the IFM motif and Phe1460 on S6_{III}. **d** Contraction of the pore domain upon fast inactivation. Left: The marked shifts of the S6_{III} and S6_{IV} induce their interface rearrangement. As a result, extensive hydrophobic interactions between S6_{III} and S6_{IV} close the wide cleft in the open pore. Right: Displacement of S6_{IV} induces the $\alpha \rightarrow \pi$ transition in S6_I to avoid steric clash. Without the rotation following the $\alpha \rightarrow \pi$ transition in S6_I, residues Ile394 and Leu498 would clash with Val1758 and Ile1759 when S6_{IV} is pushed by the IFM motif. **e** The π -helical conformation of S6_{IV} provides a more favorable environment for IFM binding at its receptor site, with the polar residue Asn1753 replaced by the hydrophobic Met1754. If this is the *bona fide* fast inactivated conformation, the S6_{IV} segment undergoes both swing and axial rotation during fast inactivation.

left). On the other side of S6_{IV}, the displacement of residues Val1758 and Ile1759 would clash with Ile394 and Leu398 on S6_I, respectively, if there were no additional conformational changes. The $\alpha \rightarrow \pi$ helical transition in the middle turn of S6_I affords the solution. The rotation of the ensuing S6_I segment turns the bulky hydrophobic chains of Ile394 and Leu398 away, repositioning Ala399 to interact with Ile1759. Another

consequence of the $\alpha \rightarrow \pi$ shift is to re-orient Phe391 to interact with Tyr1755, further shrinking the volume of the central cavity (Fig. 5d, right). The concomitant events accompanying the formation of the IFM binding site and plugging of IFM to this site quickly stop ion flow at the narrowed gate.

The above analysis shows that both S6_{III} and S6_{IV} only undergo swing motions, without axial rotation, to close the

gate. However, the “apo” channel, like in most other Na_v structures, has a glyco-diosgenin (GDN)-like density penetrating its intracellular gate. We previously analyzed in detail that this conformation, despite having a non-conductive gate, appears to be less ideal for IFM accommodation due to the placement of a polar residue Asn1753 adjacent to the hydrophobic Phe residue from IFM¹⁹ (Fig. 5c, insets). We have also observed that the S6_{IV} segment tends to adopt the π form in the presence of channel antagonists, such as Protoxin II (ProTx-II), Huwentoxin IV, and a number of small-molecule inhibitors^{19,21-23}. We have shown that the simple $\alpha \rightarrow \pi$ transition of the single segment S6_{IV} would have multiple consequences, including reshaping the IFM-binding site to a more agreeable hydrophobic cavity, further tightening the intracellular gate to an extent that is too narrow for GDN binding, and closing or narrowing the III-IV and IV-I fenestrations¹⁹.

When the PD structures of Na_v1.7V_O and the ProTx-II-bound Na_v1.7 are superimposed relative to the shoulder, the $\alpha \rightarrow \pi$ rotation in the middle of S6_{IV} is evident (Fig. 5e, left). Consequently, while the Phe in IFM pushes Asn1753 and Ile1756 away, it also attracts Met1754 to revolve toward the hydrophobic cluster formed by Phe1460, Ile and Phe in the IFM motif (Figs. 5e, right and 6a; Supplementary Video S2).

DISCUSSION

The structural analyses presented here reveal the molecular foundation for the dual actions of VTD on Na_v channels. Binding to site I stabilizes an inactivated state, consistent with the left shift of the steady-state inactivation curve when the channels are treated with VTD (Supplementary Fig. S1). Inhibition of the peak currents is likely a collective result of VTD binding to both sites, and site C binding appears to be responsible for the use-dependence of peak current reduction as well as the induced persistent currents (Fig. 1a).

The binding pose of VTD at site C is consistent with the reported observation in single-channel recording that VTD led to both reduced conductance and increased open probability^{27,28}. Channel opening may be induced when VTD is accessing site C. Then, what is the entry site? Is VTD initially docked to site I and subsequently travels to site C, or does it approach the cavity from the fenestrations or the intracellular gate? Addressing this question requires comprehensive characterizations. The static structures reported here set the framework for future computational and experimental analyses.

Uniform or diverse PD conformations in fast inactivation?

Prior to the determination of an open Na_v structure in this study, the PD has mainly displayed three non-conductive conformations among the dozens of eukaryotic Na_v structures: tight, relaxed, and loose. The PD in Na_vPaS and Na_v1.7-M11 represent the most contracted conformation, wherein the diameter of the intracellular gate is less than 2 Å^{6,12,36}. This sealed gate cannot accommodate any lipid. In a relaxed PD, exemplified by the “ π -form” of the ProTx-II- and HWTX-IV-bound Na_v1.7, the constriction site is less than 3 Å in diameter, still disallowing the penetration of a steroid-like molecule¹⁹. In the majority of the Na_v structures, the intracellular gate, with a diameter between 5–6 Å, is penetrated with a GDN-like molecule, and we refer to this state as the loose PD (Fig. 6b). Note that three similar states of the PD have been observed in Ca_v channels, although the detailed parameters, such as the gate diameter and the α or π form of the S6 segments, vary³².

Na_v1.7-M11, with its tight PD and one down VSD, may represent the CSI conformation. Does the tight PD resemble that in the resting channels? To answer this question, a *bona fide* resting-state structure is necessitated. By contrast, all four VSDs are up in the Na_v structures with relaxed or loose PD³. Then, which represents the fast inactivated conformation, the relaxed, the loose, or both? We previously suggested that the relaxed state, in which the chemical environment is more compatible with IFM insertion, may reflect the fast inactivated state. Yet, a key question concerns the steroid-like molecule in the intracellular gate in the loose conformation. If the density is only from a GDN or a cholesterol hemisuccinate, which was supplemented in high concentration during channel purification, such a conformation is, in essence, an artifact. However, is it possible that a cholesterol or steroid molecule may insert into the gate even under physiological conditions? If so, how quickly can it occur? Is it related to slow inactivation? It is noted that a recent study suggested that fast inactivation might involve rotation of the S6_{III} and S6_{IV} segments³⁷. Although no rotation of S6_{III} is observed when the structures of the open and relaxed channels are compared, the S6_{IV} segment does undergo an $\alpha \rightarrow \pi$ transition in addition to the swing motion of the helix. This observation further supports that the relaxed conformation may correspond to the fast inactivated state.

Disease mutations mapped to the inactivation segments

Because fast inactivation in Na_v channels is critical to numerous physiological processes, its mechanism has been studied for decades. Two primary models, the ball-and-chain model³⁸ and the hinged-lid model^{38,39}, have been proposed to explain the experimental data. Based on the structural comparison of Na_vPaS and EeNa_v1.4, we proposed the “door wedge” model, in which docking of the IFM motif into its receptor site allosterically drives pore closure^{6,7}. The study presented here, which reports the long-sought-after structure of an open conformation for the eukaryotic Na_v channels, provides direct evidence to support the wedge model (Fig. 6c).

In addition, we previously analyzed dozens of disease-associated mutations that are clustered into two mechanistic classes within the context of the wedge model^{40,41}. Mutations that weaken IFM-receptor interactions directly compromise the fast inactivation, and those that hinder the conformational coupling required for III-IV linker displacement and pore closure influence the process indirectly (Fig. 6d). Both perturbations would favor channel opening during prolonged depolarization, resulting in a left shift in steady-state inactivation, enhanced persistent or tail currents, and accelerated recovery from inactivation.

Determination of the open-state structure of Na_v1.7, particularly with the identification of additional coupling residues, has advanced our mechanistic understanding of many Na_v disease mutations. We will use the generic numbering³³ to describe some of the disease mutations as they have been identified in multiple Na_v subtypes. One cluster of mutations resides in the III-IV fenestration, including Phe_{S6III,40}, Met_{S6IV,31}, Ile_{S6IV,33}, and Ala_{S6IV,34}, and the other lies in the IV-I fenestration, including Asn_{S6I,30}, Leu_{S6I,33}, Tyr_{S6IV,32}, and Ile_{S6IV,33} (Fig. 6d). Y1781C/H_{S6IV,32}, I1782M/S_{S6IV,33}, and A1783T/V_{S6IV,34} have been found in patients with Na_v1.1-related DRVT, N406K/S_{S6I,30}, L409V_{S6I,33}, F1473C_{S6III,40}, M1766L_{S6IV,31}, Y1767C_{S6IV,32}, and I1768V_{S6IV,33} in Na_v1.5-associated long QT syndrome 3 (LQT3), L407F_{S6I,33} in Na_v1.6-linked developmental and epilep-

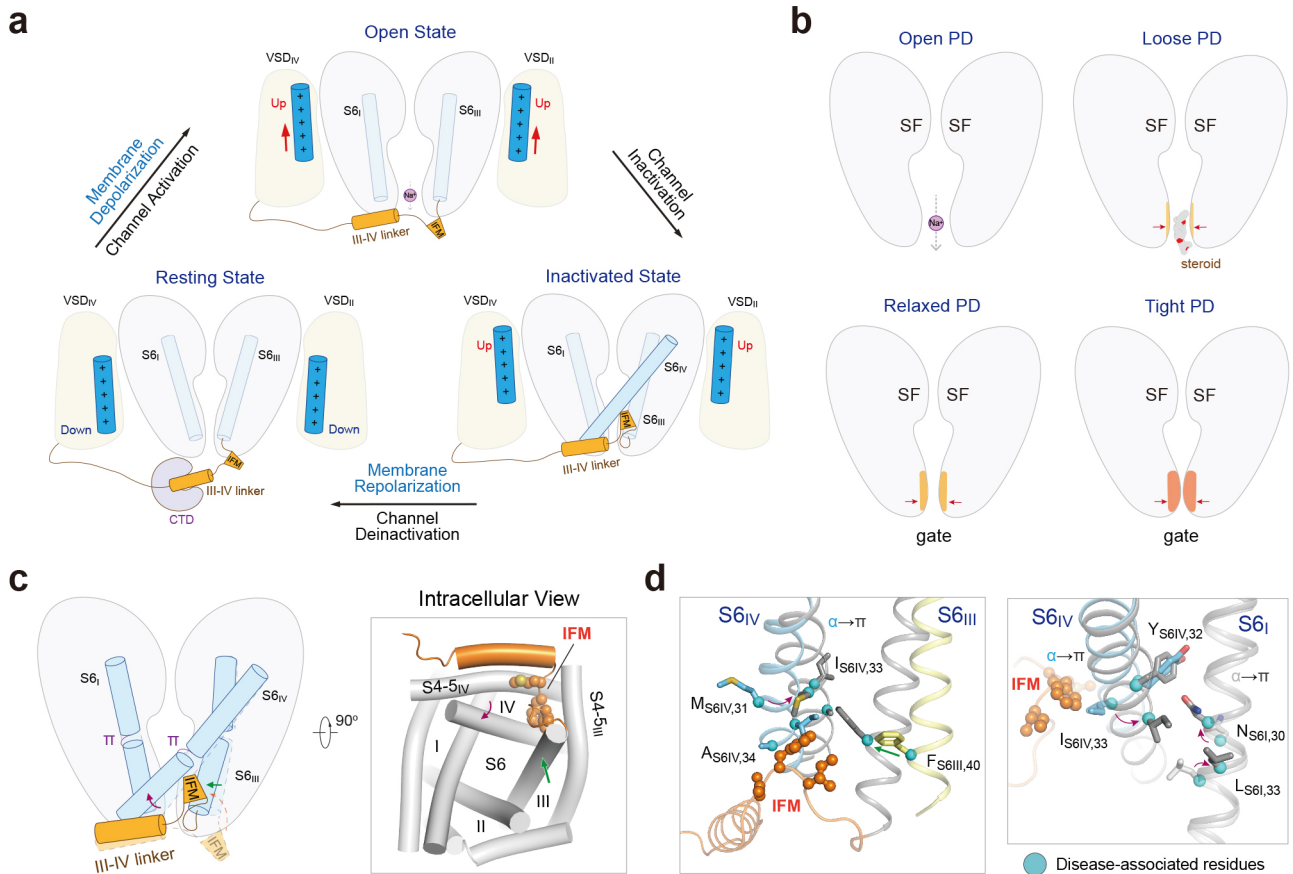


Fig. 6 The “door wedge” allosteric mechanism governing Na_v channel fast inactivation. **a** Schematic working cycle of Na_v channels in response to changes in membrane potential. **b** Schematic overview of the conformational landscape of the PD in eukaryotic Na_v channels. For visual simplicity, these distinct PD states, spanning open, loose, relaxed, and tight conformations, are highlighted by differences in the diameter of the intracellular gate in this panel. In the experimental structures, they are also distinguished by the number and size of fenestrations, and the α - or π -helical turns of the four pore-lining S6 segments. **c** Schematic illustration of the “door wedge” allosteric model for fast inactivation in Na_v channels. During fast inactivation, the IFM motif wedges towards its receptor site, pulling S6_{III} and pushing S6_{IV}. Together with the concomitant changes of S6_I and S6_{II}, the intracellular gate narrows down to cut ion flow. **d** Disease-associated hotspot mutation loci involved in conformational coupling during fast inactivation. The Ca atoms of these hotspot residues are shown as cyan spheres; some representative residues are highlighted as sticks. Generic-numbered residues correspond to the following disease mutations identified across multiple Na_v subtypes, including Y1781C/H_{S6IV,32}, I1782M/S_{S6IV,33} and A1783T/V_{S6IV,34} in Na_v 1.1-related Dravet syndrome (DRVT); N406K/S_{S6I,30}, L409V_{S6I,33}, F1473C_{S6III,40}, M1766L_{S6IV,31}, Y1767C_{S6IV,32}, I1768V_{S6IV,33} in Na_v 1.5-related LQT3; L407F_{S6I,33} in Na_v 1.6-related DEE13; and N395K_{S6I,30} and F1460V_{S6III,40} in Na_v 1.7-related primary erythralgia.

tic encephalopathy 13 (DEE13), and N395K_{S6I,30} and F1460V_{S6III,40} in Na_v 1.7-related primary erythralgia. LQT3 mutations such as Y1767C_{S6IV,32} and N406K_{S6I,30} promote elevated late I_{Na} , and all these mutations accelerate recovery from inactivation compared with WT channels, suggesting destabilization of the inactivated state⁴²⁻⁴⁵.

In sum, the structures of VTD-bound Na_v 1.7 reveal the molecular basis for the dual modulations of Na_v 1.7 by the long-studied small molecule neurotoxin. The open-conformation of VTD-potentiated Na_v 1.7 fills an important void in the structural biology of Na_v channels and establishes the framework for a detailed understanding of channel gating and fast inactivation.

MATERIALS AND METHODS

Whole cell electrophysiology

We applied a protocol similar to our previous publication with minor adjustments^{40,48-49}. All currents were recorded in HEK293T cells. Cells were transiently co-transfected with human Na_v 1.7 and eGFP using Lipofectamine 2000 (Invitrogen). Cells with green fluorescence were randomly selected for patch-clamp recordings 24–48 h after transfection. All

experiments were performed at room temperature.

Currents were recorded using an EPC10-USB amplifier with Patchmaster software v2*90.2 (HEKA Elektronik), filtered at 3 kHz (low-pass Bessel filter) and sampled at 50 kHz. The borosilicate pipettes (Sutter Instrument) used in all experiments had a resistance of 2–4 M Ω , series resistance was compensated by > 75%. The electrodes were filled with the internal solution composed of 105 mM CsF, 40 mM CsCl, 10 mM NaCl, 10 mM EGTA, and 10 mM HEPES, pH adjusted to 7.4 with CsOH. The external solution contained 140 mM NaCl, 4 mM KCl, 1.5 mM CaCl₂, 1 mM MgCl₂, 10 mM D-glucose, and 10 mM HEPES, pH adjusted to 7.4 with NaOH. The linear component of leaky currents and capacitive transients were subtracted using the P/4 procedure. Only cells with high seal resistance (> 1 G Ω) were used.

To investigate VTD’s effects on Na_v 1.7, veratridine was dissolved in dimethyl sulfoxide (DMSO, Sigma) to make a stock solution of 100 mM and stored at -20 °C. Working solutions were freshly prepared and perfused to the recording cell using a multichannel perfusion system (VM8, ALA) for several minutes until the pharmacological effect reached saturation. Prior to drug application, cells were recorded for 5–15 min to

establish a stable peak current.

To assess the inhibitory effect of VTD on the peak current, cells were held at -120 mV and depolarized to a test pulse to 0 mV for 50 ms. To investigate the use-dependent effect, a train of 30 pulses (5 -ms duration to 0 mV) was applied at 5 Hz from a holding potential of -120 mV. The accumulated tail current at the end of the stimulation was normalized to the amplitude of the first peak current. Concentration–response curves were fitted with: $Y = \text{Bottom} + (\text{Top} - \text{Bottom}) / (1 + 10^{(\text{LogIC}_{50} - X) * \text{Hill Slope}})$, where IC_{50} or EC_{50} represents the drug concentration that inhibits 50% of the peak current or activates 50% of the tail current, respectively; X is log of the drug concentration; and Hill Slope is the slope factor.

To characterize channel gating properties, voltage-dependent activation was assessed using a protocol consisting of steps from a holding potential of -120 mV to voltages ranging from -90 mV to $+80$ mV for 50 ms in 5 -mV increments. Conductance (G) was calculated as $G = I / (V - V_r)$, where V_r is the reversal potential. Normalized conductance was plotted against the test voltage (from -90 mV to $+30$ or $+40$ mV) to generate activation curves. Voltage-dependent steady-state inactivation was determined with a two-pulse protocol, in which cells were conditioned with $1,000$ -ms pre-pulses from -130 mV (or -150 mV for $\text{Na}_v1.7$ -L1449A) to 0 mV in 5 -mV increments, followed by a 50 -ms test pulse to 0 mV. Normalized peak currents were plotted against pre-pulse voltage to construct inactivation curves. Both activation and inactivation relationships were fitted with a Boltzmann function to determine the $V_{1/2}$ and slope factors (k).

To ensure data integrity, rigorous quality control criteria were applied, excluding activation curves with $(k) \leq 4$. Data were processed using Fitmaster (HEKA Elektronik), Igor Pro (WaveMetrics), and GraphPad Prism (GraphPad Software). All quantitative data are presented as mean \pm SEM, with n representing the number of independently recorded cells. Statistical significance was assessed using one-way ANOVA and the extra sum-of-squares F test.

Cell culture and transient expression of human $\text{Na}_v1.7$ complex in HEK293F cells

The proteins were expressed using the same codon-optimized constructs from our previous work, specifically human $\text{Na}_v1.7$ (Uniprot Q15858), $\beta 1$ subunit (Uniprot Q07699), and $\beta 2$ subunit (Uniprot O60939) in pCAG expression vector. HEK293F cells (Thermo Fisher Scientific, R79007) were maintained in SMM 293T-II medium (Sino Biological Inc.) at 37°C under 5% CO_2 and 60% humidity. For transient expression of the human $\text{Na}_v1.7$ complex, each liter of culture at a density of 1.5 – 2.0×10^6 cells per mL was transfected with a mixture of 2.5 mg plasmids, including 1.5 mg $\text{Na}_v1.7$, 0.5 mg $\beta 1$, and 0.5 mg $\beta 2$. The plasmid mixture was pre-incubated with 4 mg 40 -kDa linear PEI (Polysciences) in 50 mL fresh medium for 15 – 30 min.

Protein purification of human $\text{Na}_v1.7$ -VTD complexes

Transfected HEK293F cells (24 L) were harvested ~ 48 h post-transfection by centrifugation at $3,600\times g$ for 10 min and resuspended in lysis buffer containing 25 mM Tris-HCl (pH 7.5) and 150 mM NaCl. The suspension was supplemented with 0.1 μM VTD (MCE), 2 mM PMSF, and protease inhibitor cocktail (Selleckchem), followed by incubation at 4°C with gentle rotation for 30 min. n -Dodecyl- β -D-maltopyranoside (DDM, Anatrace) was then added to a final concentration of 1% (w/v), along with cholesteryl hemisuccinate Tris salt (CHS,

Anatrace) at 0.1% (w/v). The mixture was incubated at 4°C for an additional 2 h. The supernatant obtained by centrifugation at $16,000\times g$ for 45 min was applied to anti-FLAG M2 affinity resin (Sigma) and incubated for batch binding. The resin was washed four times with wash buffer (buffer W) containing 25 mM Tris-HCl (pH 7.5), 150 mM NaCl, 0.06% GDN, 0.1 μM VTD, and protease inhibitors. Bound proteins were eluted with buffer W supplemented with 0.2 mg/mL FLAG peptide (GenScript). The eluent was subsequently passed through Strep-Tactin Sepharose resin (IBA) by gravity flow, washed four times with buffer W, and eluted with buffer W containing 2.5 mM desthiobiotin. The final eluate was concentrated using a 100 -kDa molecular weight cut-off Amicon filter unit (Millipore) and subjected to size-exclusion chromatography on a Superose 6 $10/300$ GL column (GE Healthcare) pre-equilibrated in buffer containing 25 mM Tris-HCl (pH 7.5), 150 mM NaCl, 0.02% GDN, and 0.1 mM veratridine. The peak fractions were pooled supplemented with 0.5 mM veratridine and incubated at 4°C for 30 min; then concentrated to ~ 10 mg/mL for cryo-grid preparation.

Cryo-EM sample preparation and data acquisition

UltrAuFoil (R1.2/1.3 300 mesh, Quantifoil) grids were glow-discharged with easiGlow (PELCO) using 15 mA for 15 s at 0.37 mBar. Vitrobot Mark IV chamber was pre-cooled to 10°C with 100% humidity. 3 μL concentrated $\text{Na}_v1.7$ -VTD was applied to a freshly treated grid, which was then blotted with filter paper for 4 s and plunged into liquid ethane cooled by liquid nitrogen. Grids were loaded to a 300 kV Titan Krios G3i with spherical aberration (Cs) image corrector (Thermo Fisher Scientific). Micrographs were automated recorded in SerialEM by a GIF Quantum K2 Summit camera (Gatan) with a 20 eV slit in super-resolution mode at a nominal magnification of $105,000\times$, resulting in a calibrated pixel size of 0.557 \AA . Each movie stack was exposed for 5.6 s (0.175 s per frame, 32 frames) with a total electron dose of ~ 50 $\text{e}^-/\text{\AA}^2$. The movie stacks were aligned, summed and dose-weighted using Warp⁵⁰ and binned to a pixel size of 1.114 \AA per pixel.

Data processing

A total of $5,021$ micrographs were collected and pre-processed on-the-fly in Warp⁵⁰, then imported into cryoSPARC⁵¹. Particles from 100 micrographs were initially auto-picked using blob picking and subjected to 2D classification to generate templates. Class averages displaying clear features were selected for template-based particle picking for the full dataset and *Ab-initio* reconstruction. Picked and extracted bin4 particles were further cleaned via 2D classification to remove obvious junk. The cleaned dataset was subjected to heterogeneous refinement using two initial references derived from *Ab-initio* reconstruction. Bin2 particles were re-extracted from selected good class, followed by four rounds of heterogeneous refinement and duplicate removal. The best-resolved class was extracted into bin1 for further processing. The selected particles were subjected to two additional rounds of heterogeneous refinement incorporating higher-resolution features. Subsequent non-uniform refinement of the dominant class, comprising $631,118$ particles, yielded a reconstruction at an overall resolution of 2.7 \AA . In this reconstruction, the S6_{III} segment exhibited branched density, suggesting a mixed conformational state. To resolve structural heterogeneity, unsupervised 3D classification was performed on the $631,118$ particles without providing multi-

ple manually defined references. A range of different initial resolution filters and class numbers, with “force hard classification” enabled, was tried. Classification with a 6 Å low-pass filter and four output classes successfully resolved three distinct conformational states: the open state, the site I-bound state, and the apo state. The resulting 3D classes were subsequently used as references for heterogeneous refinement, followed by a final round of non-uniform refinement. Final reconstructions were obtained at overall resolutions of 2.9 Å for the open state (133,758 particles, 21.2%), 2.7 Å for the site I-bound state (335,177 particles, 53.1%), and 2.9 Å for the apo state (162,183 particles, 25.7%).

Model building and refinement

The published apo-state structure (PDB: 7w9k) was applied as the initial model for hNav_v1.7-VTD complexes and underwent manual inspection and adjustments in COOT⁵². The VTD molecules were then modeled and refined based on the density in COOT⁵². Subsequent refinement was performed using the real-space refinement in PHENIX⁵³, followed by molecular dynamics-based optimization in ISOLDE⁵⁴. A final round of real-space refinement in PHENIX⁵³ was conducted to complete and validate the model. Validation results are detailed in Supplementary Table S5.

MDS

The protein models were built with our cryo-EM structures of hNav1.7V_O, hNav1.7 apo, and the previously resolved structure rNav1.5-QQQ (PDB: 7FBS), as well as its rebuilt version. Only the PDs (residue 233–409, 850–977, 1306–1463, and 1629–1769 in Na_v1.7, and residue 236–429, 824–945, 1320–1481, and 1644–1777 in Na_v1.5) were included in the simulation systems. CHARMM-GUI⁵⁵ was used to build the simulation systems. The protein models were embedded into a POPC lipid bilayer. After membrane insertion, the system was solvated in 0.15 M NaCl solution. The simulation box was around 10 × 10 × 12 nm³, which comprised ~120,000 atoms.

We performed MDS with GROMACS⁵⁶ version 2021.2, using the CHARMM36m force field⁵⁷ and CHARMM TIP3P water model. For all the production simulations, the time step was 2 fs. The v-rescale algorithm with a time constant of 0.5 ps was used to maintain the temperature at 310 K⁵⁸, and the Parrinello-Rahman algorithm with a time constant of 5 ps was used to maintain the pressure at 1 bar⁵⁹. The Particle-Mesh Ewald method was used to calculate long-range electrostatics with a cut-off of 1.2 nm⁶⁰, and the van der Waals interactions were smoothly switched off from 1.0 nm to 1.2 nm. The bonds involving hydrogen were constrained using the LINCS algorithm⁶¹. The MDAnalysis package⁶² was used to analyze the MDS results. PyMOL was used to render molecular visualizations³⁰. The default CHARMM-GUI protocol was used to progressively equilibrate the system, including 5,000 steps of energy minimization, 250 ps NVT equilibration, and 1,625 ps NPT equilibration. Then we restrained the Ca atoms of the protein with a force constant of 1,000 kJ/mol/nm² to perform another 100 ns NPT equilibration. For production simulations, we relaxed the restraints of the pore helix (10 residues before and after the DEKA locus in the SF), while the Ca atoms in other regions were still restrained. We performed ion permeation simulations by applying an electric field of 0.01 V/nm along the pore axis pointing to the intracellular direction, which generated a transmembrane potential of ~120 mV. Three replicates of 1.5 μs simulations were performed for

each simulation system.

Water distribution analysis

The water distribution around the intracellular gate was estimated from production simulation trajectories. The origin was assigned as the mean position of the four Ca atoms of DEKA locus, and then the pore axis was assigned as the z-axis. By binning the z-axis into 2 Å grid and calculating the number of water molecules around 1 nm of the pore axis, we obtained the water density distribution along the z-axis from the following equation:

$$\rho = \frac{N}{V} = \frac{N}{\pi r^2 \Delta z}$$

where ρ is water density, N is the number of water molecules observed in the cylinder layer, V is the volume of the cylinder layer, r (= 1 nm) is the radius of the cylinder, Δz (= 2 Å) is the grid-spacing. Then the density distribution was normalized by the water density in bulk solution.

Ion permeation analysis

The permeation events were determined by analyzing the z coordinates of ion trajectories: if an ion moved from the extracellular side across the membrane to the intracellular side, one permeation event was counted. By counting the number of permeation events, the conductance of the channel for ion (g_{ion}) can be calculated as follows:

$$g_{\text{ion}} = \frac{I}{V} = \frac{N_p Q_{\text{ion}}}{tV} = \frac{N_p Q_{\text{ion}}}{tEL_z}$$

where N_p is the observed number of permeation events, Q_{ion} is the charge of the permeating ion, t is the simulation time, V is the transmembrane potential, E is the applied electric field, and L_z is the box size in the z direction. Errors were estimated by the standard deviations of three replicates.

Distribution analysis of permeating ions at the gate

To evaluate the asymmetry of the permeation pathway, we analyzed the spatial distribution of permeant ions around the gate region. This analysis selected ions located between $z = -30$ and -15 Å and within 10 Å of the pore axis, then we projected their coordinates onto the membrane plane. This 2D x-y distribution was normalized to its maximum value to obtain a relative probability.

DATA AVAILABILITY

The data that support this study are available from the corresponding authors upon reasonable request. The cryo-EM maps have been deposited in the Electron Microscopy Data Bank under accession codes EMD-67990 (Na_v1.7V_O) and EMD-67991 (Na_v1.7V_I). The corresponding atomic coordinates have been deposited in the Protein Data Bank under accession codes 21TP (Na_v1.7V_O) and 21TQ (Na_v1.7V_I).

AUTHOR CONTRIBUTIONS

N.Y., J.H., and X.F. conceived the project. X.F., J.C., L.X., H.W., T.W., X.H., F.L., X.J., C.S., J.H., and N.Y. designed experiments. X.F. and J.H. performed all experiments related to cryo-EM studies, including protein expression, purification, and 3D reconstructions. J.C. carried out experiments related to electrophysiology. L.X. performed MDS. X.H. and F.L. prepared the mutant plasmids. X.F., J.C., L.X., H.W., T.W., X.H., F.L., X.J., C.S., J.H., and N.Y. discussed and analyzed data. X.F., J.H., and N.Y. wrote the manuscript with input from all authors. All

authors approved the final manuscript.

ACKNOWLEDGEMENTS

We thank the cryo-EM facility at Princeton Imaging and Analysis Centre for technical support. Data analysis was supported by the Biomedical Data Center of Shenzhen Medical Academy of Research and Translation (SMART) and the Tiger cluster in Princeton University. This work was funded by the National Natural Science Foundation of China (32271252 to N.Y. and 32501081 to J.H.). J.H. and X.F. are supported by the start-up funds from SMART, and X.F. was supported by the HFSP long-term fellowship (LT000754/2020-L) from the International Human Frontier Science Program Organization (HFSP) from 2020 to 2023. X.J. is supported by Beijing Natural Science Foundation (7264373).

COMPETING INTERESTS

The authors declare no competing interests.

REFERENCES

- Hille, B. Ion channels of excitable membranes. 3rd Edition. Sunderland: Sinauer Associates (2001).
- Hodgkin, A.L. & Huxley, A.F. Resting and action potentials in single nerve fibres. *J. Physiol.* **104**, 176–195 (1945).
- Huang, J., Pan, X.J. & Yan, N. Structural biology and molecular pharmacology of voltage-gated ion channels. *Nat. Rev. Mol. Cell Biol.* **25**, 904–925 (2024).
- Liao, M.F., Cao, E.H., Julius, D. & Cheng, Y.F. Structure of the TRPV1 ion channel determined by electron cryo-microscopy. *Nature* **504**, 107–112 (2013).
- Kühlbrandt, W. The resolution revolution. *Science* **343**, 1443–1444 (2014).
- Shen, H.Z. et al. Structure of a eukaryotic voltage-gated sodium channel at near-atomic resolution. *Science* **355**, eaal4326 (2017).
- Yan, Z. et al. Structure of the Na_v1.4-β1 complex from electric eel. *Cell* **170**, 470–482.e11 (2017).
- Pan, X.J. et al. Structure of the human voltage-gated sodium channel Na_v1.4 in complex with β1. *Science* **362**, eaau2486 (2018).
- Jiang, D.H. et al. Structural basis for voltage-sensor trapping of the cardiac sodium channel by a deathstalker scorpion toxin. *Nat. Commun.* **12**, 128 (2021).
- Clairfeuille, T. et al. Structural basis of α-scorpion toxin action on Na_v channels. *Science* **363**, eaav8573 (2019).
- Jiang, D.H. et al. Open-state structure and pore gating mechanism of the cardiac sodium channel. *Cell* **184**, 5151–5162.e11 (2021).
- Huang, G.X.Y. et al. Unwinding and spiral sliding of S4 and domain rotation of VSD during the electromechanical coupling in Na_v1.7. *Proc. Natl. Acad. Sci. USA* **119**, e2209164119 (2022).
- Li, Z.Q. et al. Dissection of the structure-function relationship of Na_v channels. *Proc. Natl. Acad. Sci. USA* **121**, e2322899121 (2024).
- Cox, J.J. et al. An SCN9A channelopathy causes congenital inability to experience pain. *Nature* **444**, 894–898 (2006).
- Cummins, T.R., Dib-Hajj, S.D. & Waxman, S.G. Electrophysiological properties of mutant Na_v1.7 sodium channels in a painful inherited neuropathy. *J. Neurosci.* **24**, 8232–8236 (2004).
- Nassar, M.A. et al. Nociceptor-specific gene deletion reveals a major role for Na_v1.7 (PN1) in acute and inflammatory pain. *Proc. Natl. Acad. Sci. USA* **101**, 12706–12711 (2004).
- Yang, Y. et al. Mutations in SCN9A, encoding a sodium channel alpha subunit, in patients with primary erythralgia. *J. Med. Genet.* **41**, 171–174 (2004).
- Shen, H.Z., Liu, D.L., Wu, K., Lei, J.L. & Yan, N. Structures of human Na_v1.7 channel in complex with auxiliary subunits and animal toxins. *Science* **363**, 1303–1308 (2019).
- Huang, G.X.Y. et al. High-resolution structures of human Na_v1.7 reveal gating modulation through α-π helical transition of S6_{IV}. *Cell Rep.* **39**, 110735 (2022).
- Zhang, J.T. et al. Structural basis for Na_v1.7 inhibition by pore blockers. *Nat. Struct. Mol. Biol.* **291**, 208–1216 (2022).
- Wu, Q.R. et al. Structural mapping of Na_v1.7 antagonists. *Nat. Commun.* **14**, 3224 (2023).
- Huang, J. et al. Cannabidiol inhibits Na_v channels through two distinct binding sites. *Nat. Commun.* **14**, 3613 (2023).
- Huang, J., Fan, X., Jin, X.Q., Teng, L.M. & Yan, N. Dual-pocket inhibition of Na_v channels by the antiepileptic drug lamotrigine. *Proc. Natl. Acad. Sci. USA* **120**, e2309773120 (2023).
- Sutro, J.B. Kinetics of veratridine action on Na channels of skeletal muscle. *J. Gen. Physiol.* **87**, 1–24 (1986).
- Leibowitz, M.D., Sutro, J.B. & Hille, B. Voltage-dependent gating of veratridine-modified Na channels. *J. Gen. Physiol.* **87**, 25–46 (1986).
- Ulbricht, W. The effect of veratridine on excitable membranes of nerve and muscle. In: Brown, L. et al. eds. *Reviews of physiology, biochemistry and pharmacology* 61. Berlin, Heidelberg: Springer, 18–71 (1969).
- Wang, G., Dugas, M., Armah, B.I. & Honerjäger, P. Sodium channel comodification with full activator reveals veratridine reaction dynamics. *Mol. Pharmacol.* **37**, 144–148 (1990).
- Barnes, S. & Hille, B. Veratridine modifies open sodium channels. *J. Gen. Physiol.* **91**, 421–443 (1988).
- Zhang, X.Y., Bi, R.Y., Zhang, P. & Gan, Y.H. Veratridine modifies the gating of human voltage-gated sodium channel Na_v1.7. *Acta Pharmacol. Sin.* **39**, 1716–1724 (2018).
- DeLano, W.L. The PyMOL molecular graphics system. <https://cir.nii.ac.jp/crid/1571980075906330880> (2002).
- Fan, X. et al. Phrixotoxin-3 binds to three distinct antagonistic sites on human Na_v1.6. *Cell Res.* **35**, 610–613 (2025).
- Gao, S. et al. Structural basis for human Ca_v1.2 inhibition by multiple drugs and the neurotoxin calciseptine. *Cell* **186**, 5363–5374.e16 (2023).
- Jin, X.Q., Huang, J., Wang, H., Wang, K. & Yan, N. A versatile residue numbering scheme for Na_v and Ca_v channels. *Cell Chem. Biol.* **31**, 1394–1404 (2024).
- Weiss, R.E. & Horn, R. Functional differences between two classes of sodium channels in developing rat skeletal muscle. *Science* **233**, 361–364 (1986).
- Liu, Y.C., Bassetto, C.A.Z. Jr., Pinto, B.I. & Bezanilla, F. A mechanistic reinterpretation of fast inactivation in voltage-gated Na⁺ channels. *Nat. Commun.* **14**, 5072 (2023).
- Shen, H.Z. et al. Structural basis for the modulation of voltage-gated sodium channels by animal toxins. *Science* **362**, eaau2596 (2018).
- Liu, Y. et al. Molecular basis of sodium channel inactivation. *Nat. Commun.* **16**, 10565 (2025).
- Armstrong, C.M., Bezanilla, F. & Rojas, E. Destruction of sodium conductance inactivation in squid axons perfused with pronase. *J. Gen. Physiol.* **62**, 375–391 (1973).
- West, J.W. et al. A cluster of hydrophobic amino acid residues required for fast Na⁺-channel inactivation. *Proc. Natl. Acad. Sci. USA* **89**, 10910–10914 (1992).
- Li, Z.Q. et al. Structure of human Na_v1.5 reveals the fast inactivation-related segments as a mutational hotspot for the long QT syndrome. *Proc. Natl. Acad. Sci. USA* **118**, e2100069118 (2021).
- Pan, X.J. et al. Comparative structural analysis of human Na_v1.1 and Na_v1.5 reveals mutational hotspots for sodium channelopathies. *Proc. Natl. Acad. Sci. USA* **118**, e2100066118 (2021).
- Hu, R.M. et al. Mexiletine rescues a mixed biophysical phenotype of the cardiac sodium channel arising from the SCN5A mutation, N406K, found in LQT3 patients. *Channels* **12**, 176–186 (2018).
- Itoh, H., Shimizu, M., Takata, S., Mabuchi, H. & Imoto, K. A novel missense mutation in the SCN5A gene associated with Brugada syndrome bidirectionally affecting blocking actions of antiarrhythmic drugs. *J. Cardiovasc. Electrophysiol.* **16**, 486–493 (2005).
- Huang, H., Priori, S.G., Napolitano, C., O’Leary, M.E. & Chahine, M. Y1767C, a novel SCN5A mutation, induces a persistent Na⁺ current and potentiates ranolazine inhibition of Na_v1.5 channels. *Am. J. Physiol. Heart Circ. Physiol.*

- 300, H288–H299 (2011).
45. Clancy, C.E., Tateyama, M., Liu, H.J., Wehrens, X.H.T. & Kass, R.S. Non-equilibrium gating in cardiac Na⁺ channels: an original mechanism of arrhythmia. *Circulation* **107**, 2233–2237 (2003).
 46. Meng, E.C., Pettersen, E.F., Couch, G.S., Huang, C.C. & Ferrin, T.E. Tools for integrated sequence-structure analysis with UCSF Chimera. *BMC Bioinformatics* **7**, 339 (2006).
 47. Smart, O.S., Neduveilil, J.G., Wang, X.N., Wallace, B.A. & Sansom, M.S.P. HOLE: a program for the analysis of the pore dimensions of ion channel structural models. *J. Mol. Graph.* **14**, 354–360 (1996).
 48. Huang, X.S. et al. Structural basis for high-voltage activation and subtype-specific inhibition of human Na_v1.8. *Proc. Natl. Acad. Sci. USA* **119**, e2208211119 (2022).
 49. Fan, X., Huang, J., Jin, X.Q. & Yan, N. Cryo-EM structure of human voltage-gated sodium channel Na_v1.6. *Proc. Natl. Acad. Sci. USA* **120**, e2220578120 (2023).
 50. Tegunov, D. & Cramer, P. Real-time cryo-electron microscopy data preprocessing with Warp. *Nat. Methods* **16**, 1146–1152 (2019).
 51. Punjani, A., Rubinstein, J.L., Fleet, D.J. & Brubaker, M.A. cryoSPARC: algorithms for rapid unsupervised cryo-EM structure determination. *Nat. Methods* **14**, 290–296 (2017).
 52. Emsley, P., Lohkamp, B., Scott, W.G. & Cowtan, K. Features and development of Coot. *Acta Crystallogr. D Biol. Crystallogr.* **66**, 486–501 (2010).
 53. Afonine, P.V. et al. Towards automated crystallographic structure refinement with *phenix.refine*. *Acta Crystallogr. D Biol. Crystallogr.* **68**, 352–367 (2012).
 54. Croll, T.I. ISOLDE: a physically realistic environment for model building into low-resolution electron-density maps. *Acta Crystallogr. D Struct. Biol.* **74**, 519–530 (2018).
 55. Jo, S., Kim, T., Iyer, V.G. & Im, W. CHARMM-GUI: a web-based graphical user interface for CHARMM. *J. Comput. Chem.* **29**, 1859–1865 (2008).
 56. Abraham, M.J. et al. GROMACS: high performance molecular simulations through multi-level parallelism from laptops to supercomputers. *SoftwareX* **1–2**, 19–25 (2015).
 57. Huang, J. et al. CHARMM36m: an improved force field for folded and intrinsically disordered proteins. *Nat. Methods* **14**, 71–73 (2017).
 58. Bussi, G., Donadio, D. & Parrinello, M. Canonical sampling through velocity rescaling. *J. Chem. Phys.* **126**, 014101 (2007).
 59. Parrinello, M. & Rahman, A. Polymorphic transitions in single crystals: a new molecular dynamics method. *J. Appl. Phys.* **52**, 7182–7190 (1981).
 60. Darden, T., York, D. & Pedersen, L. Particle mesh Ewald: an $N \cdot \log(N)$ method for Ewald sums in large systems. *J. Chem. Phys.* **98**, 10089–10092 (1993).
 61. Hess, B., Bekker, H., Berendsen, H.J.C. & Fraaije, J.G.E.M. LINCS: a linear constraint solver for molecular simulations. *J. Comput. Chem.* **18**, 1463–1472 (1997).
 62. Michaud-Agrawal, N., Denning, E.J., Woolf, T.B. & Beckstein, O. MDAAnalysis: a toolkit for the analysis of molecular dynamics simulations. *J. Comput. Chem.* **32**, 2319–2327 (2011).

ADDITIONAL INFORMATION

Supplementary information The online version contains supplementary material available at <https://doi.org/10.15302/vita.2026.01.0003>.

Correspondence and requests for materials should be addressed to Xiao Fan, Chen Song, Jian Huang or Nieng Yan.

Reprints and permission information is available at <https://www.vita-journal.com/>.

© The Author(s) 2026. Published by Higher Education Press. This is an Open Access article distributed under the terms of the CC BY license (<https://creativecommons.org/licenses/by/4.0/>).